

# Perovskite crystallization control via an engineered self-assembled monolayer in perovskite–silicon tandem solar cells

Received: 14 April 2025

Accepted: 16 September 2025

Published online: 20 October 2025

 Check for updates

Daoyong Zhang<sup>1,5</sup>, Boning Yan<sup>2,5</sup>, Rui Xia<sup>3,5</sup>, Biao Li<sup>1</sup>, Ruilin Li<sup>1</sup>, Pengjie Hang<sup>1</sup>✉, Haimeng Xin<sup>1</sup>, Jiyao Wei<sup>1</sup>, Ming Lei<sup>2</sup>✉, Yifeng Chen<sup>3</sup>, Jifan Gao<sup>3</sup>✉, Hengyu Zhang<sup>1</sup>, Zhenyi Ni<sup>1</sup>, Deren Yang<sup>1,4</sup>✉ & Xuegong Yu<sup>1,4</sup>✉

Buried defects at the interface between the wide-bandgap perovskite and the self-assembled monolayer (SAM) limit the performance of p–i–n solar cells, particularly in textured monolithic perovskite–silicon tandem solar cells. Here we reveal that uncontrolled perovskite crystallization dynamics on conventional SAMs drives the co-evolution of electronic defects and morphological degradation at the buried interface. This stems from structural and energetic incompatibility between the perovskite precursor solution and the SAM. To precisely control the perovskite crystallization, we develop a tailored SAM that mitigates defect formation and enhances interfacial electronic coupling. Integrated into a perovskite–silicon tandem solar cell, this approach enables a power conversion efficiency of 33.86% (certified as 33.59%) for a device with a 1-cm<sup>2</sup> area and a power conversion efficiency of 29.25% (certified as 28.53%) for an area of 16 cm<sup>2</sup>. The tandem device demonstrates remarkable operational stability, retaining more than 90% of the initial power conversion efficiency after 2,000 h of operational under 1-sun illumination.

The pursuit of higher photovoltaic efficiency has accelerated the development of perovskite–silicon tandem solar cells, which exploit the complementary bandgaps of perovskites and silicon to optimize light absorption and energy conversion<sup>1–3</sup>. Inverted perovskite architectures with self-assembled monolayers (SAMs) as hole transport layers are particularly promising for monolithic integration with textured silicon bottom cells, due to their photoelectric compatibility and scalable processing<sup>4–6</sup>. Recent advances in SAM design have demonstrated that molecular polarity regulation, anchoring engineering and functional group modification can significantly improve

interfacial order, perovskite crystallization and defect passivation<sup>7–13</sup>. For instance,  $\pi$ -system expansion via benzene rings in phosphate-based SAMs strengthens molecular dipole moments, improving substrate anchoring and charge transport<sup>7,9</sup>, whereas asymmetric or hybrid SAM systems promote phase homogeneity in perovskites<sup>14–16</sup>.

However, the buried SAM–perovskite interface demands precise control over crystallization dynamics to mitigate interfacial defect proliferation, a critical challenge exacerbated by mismatched interfacial growth and solvent residue entrapment during solution processing<sup>13,17</sup>. These defects degrade device efficiency and operational stability, with

<sup>1</sup>State Key Laboratory of Silicon and Advanced Semiconductor Materials and School of Materials Science & Engineering, Zhejiang University, Hangzhou, China. <sup>2</sup>Department of Chemistry, Zhejiang University, Hangzhou, China. <sup>3</sup>State Key Laboratory of Photovoltaic Science and Technology, Trina Solar Co. Ltd, Changzhou, China. <sup>4</sup>Institute of Information and Functional Materials, ZJU-Hangzhou Global Scientific and Technological Innovation Center, Hangzhou, China. <sup>5</sup>These authors contributed equally: Daoyong Zhang, Boning Yan, Rui Xia. ✉e-mail: [hangpengjie@zju.edu.cn](mailto:hangpengjie@zju.edu.cn); [leiming@zju.edu.cn](mailto:leiming@zju.edu.cn); [jifan.gao@trinasolar.com](mailto:jifan.gao@trinasolar.com); [mseyang@zju.edu.cn](mailto:mseyang@zju.edu.cn); [yuxuegong@zju.edu.cn](mailto:yuxuegong@zju.edu.cn)

textured silicon surfaces further amplifying interfacial disorder<sup>18,19</sup>. Conventional SAMs like [2-(9H-carbazol-9-yl)ethyl]phosphonic acid (2PACz) exhibit limited compatibility with perovskite precursor solutions, resulting from disordered molecular packing and weak interfacial anchoring or passivation<sup>20,21</sup>. This incompatibility derives uncontrollable and unhomogenized perovskite crystallization to form a relatively rough and defective buried surface<sup>22</sup>, as well as poor defect passivation to such a surface<sup>23</sup>. Note that rapid downward crystallization<sup>24</sup> of one-step perovskite deposition can easily leave residue dimethyl sulfoxide (DMSO) solvent at the buried surface, which degrades perovskites to expose the defective surface<sup>17</sup>. This issue is magnified in Br-incorporated wide-bandgap perovskites, where lattice contraction from Br<sup>-</sup>/I<sup>-</sup> alloying promotes halide segregation and accelerates defect formation thermodynamically<sup>25,26</sup>. Our studies reveal that rapid and unguided perovskite crystallization on 2PACz results in the formation of numerous nanoscale voids and lead iodide (PbI<sub>2</sub>) segregations at the buried perovskite surface, correlating with the emergence of deep-level defect traps.

Beyond crystallization control, SAM stability is equally critical for long-term device performance. Conventional carbazole-based SAMs (for example, 2PACz) suffer from molecular degradation under operational stresses, including thermal cycling and electric-field-induced desorption<sup>27</sup>. Recent studies highlight that core structure optimization, such as replacing carbazole with *peri*-fused polyaromatic cores, can enhance intrinsic molecular stability, thereby improving device longevity<sup>28</sup>. Additionally, covalent anchoring strategies (for example, trimethoxysilane-based SAMs) reinforce interfacial binding, mitigating SAM displacement during perovskite processing<sup>29</sup>.

To address these issues, we implemented buried interface engineering to regulate perovskite crystallization. This approach prioritizes structural and energetic compatibility between the perovskites and SAM substrate, achieved through the strategic modification of SAM molecular packing and their interactions with perovskites. Specifically, our SAM molecular design prioritized intrinsic molecular stability and packing regularity<sup>7,30</sup>. We used rigid conjugated linkers to enhance conductivity and dipole moments, strengthening hole extraction. Although methoxy groups enhance perovskite interfacial contact, direct attachment to a carbazole is suboptimal. We, therefore, replaced the terminal methoxy with a 1,3-dimethoxybenzene moiety, which acts as an electronic buffer to mitigate instability and preserves the beneficial electron-donating character. By optimizing  $\pi$ -orbital alignment and interfacial coordination of the SAM substrate, we suppressed defect-inducing crystallization pathways, enabling controllable perovskite growth with halide homogenization. The engineered buried interface eliminated nanovoids and PbI<sub>2</sub> segregations, with suppressed defects at the buried surface of wide-bandgap perovskites. Single-junction solar cells utilizing this strategy achieved a high power conversion efficiency (PCE) of 24.36%, whereas monolithic perovskite-silicon tandem solar cells reached a champion PCE of 33.86% (1 cm<sup>2</sup>) and 29.25% (16 cm<sup>2</sup>), demonstrating scalability. Besides, the 1-cm<sup>2</sup> tandem exhibited enhanced stability, maintaining over 90% of the initial PCE after 2,000 h of continuous maximum power point (MPP) tracking under 1-sun illumination at the ambient temperature.

## Results and discussion

### Molecular arrangements of SAMs for perovskite crystallization control

The molecular arrangement of SAMs plays a critical role in defining the buried interface quality of the perovskite film via regulating perovskite crystallization dynamics. To elucidate this relationship, we investigated two contrasting SAMs: (1) conventional 2PACz (Fig. 1a), comprising a carbazole core with a single flexible alkyl chain, and (2) [4-(3,6-bis(3,5-dimethoxyphenyl)-9H-carbazol-9-yl)phenyl]phosphonic acid (DMPP)—a modified SAM incorporating structural motifs including a rigid conjugated linker along with functionalized -OCH<sub>3</sub>

groups strategically positioned at the meta-sites to regulate interfacial molecular packing and interactions. This meta-substitution pattern (Supplementary Fig. 1) was chosen for optimal geometric matching with the perovskite lattice, where adjacent diagonal Pb atoms (-9.0 Å) and farther Pb pairs (-14.3 Å) align closely with the spacings of 9.6 Å and 14.9 Å of DMPP's methoxy groups, respectively, enabling the effective passivation of undercoordinated Pb<sup>2+</sup> sites. The DMPP SAM was engineered to address the limitations of disordered SAM-perovskite interactions by prioritizing spatial alignment and coordination compatibility. The powder colour of the two SAMs and their solubilities are compared in Supplementary Fig. 2 and Supplementary Table 1.

Density functional theory (DFT)-optimized geometries reveal striking differences in molecular anchoring configurations (Fig. 1c and Supplementary Fig. 3). Although 2PACz tends to collapse onto indium tin oxides (ITOs) with a near-planar orientation, DMPP adopts a vertically aligned configuration via -PO(OH)<sub>2</sub> bonding to ITOs, enforced by its rigid conjugated benzene ring linker. The extended  $\pi$ -conjugation system<sup>18</sup> further reinforces upright assembly through intermolecular  $\pi$ - $\pi$  interactions and an increased dipole moment (Supplementary Fig. 4). Consequently, DMPP achieves superior interfacial binding energy (-1.62 eV) compared with both collapsed (-0.88 eV) and upright (-0.78 eV) 2PACz configurations.

X-ray photoelectron spectroscopy (XPS; Fig. 1d-g and Supplementary Table 1) quantitatively corroborates these structural distinctions. The area ratio of In-O-P/In-O-H/C-O peak for DMPP<sup>13,31</sup> (25.7%; Fig. 1f) is significantly higher over 2PACz (only In-O-P/In-O-H signals, 15.9%; Fig. 1d). This difference provides clear evidence of DMPP's superior anchoring stability<sup>29</sup>. Furthermore, after rigorous dimethylformamide (DMF) washing tests (Fig. 1e,g), DMPP maintains 96.7% of its original SAM signal, whereas 2PACz retains only 87.2% of its initial coverage. These results corroborate the computational findings, demonstrating that the enhanced anchoring of conjugated DMPP arises from their dense and ordered molecular assembly, which enforces fixed molecular orientations to strengthen intermolecular interactions and assembly stability. Such interaction differences directly correlate with molecular packing order, as evidenced by grazing-incidence wide-angle X-ray scattering characterization<sup>32,33</sup> (Fig. 1h). Although 2PACz films exhibit no diffraction peak signal, indicative of a random orientation, DMPP films display three significant Bragg peaks along the out-of-plane direction, signifying locally ordered molecular alignment. Polarized Raman spectroscopy (Fig. 1i,j) quantifies this ordering through azimuthal intensity variations: DMPP achieves obvious intensity variation for both fingerprint -OCH<sub>3</sub> signal and C=C stretching versus little variation of C=C stretching for 2PACz, confirming in-plane molecular anisotropy.

The schematic models shown in Fig. 1k visualize this interfacial dichotomy in which 2PACz molecules exhibit mixed orientations (collapsed, tilted and partially upright), whereas DMPP molecules form tightly packed vertical arrays stabilized by the  $\pi$ - $\pi$  interactions. The ordered assembly of DMPP translates to homogeneous surface electronic properties. Kelvin probe force microscopy (KPFM; Supplementary Fig. 5) mapping reveals reduced potential fluctuations, whereas conductive atomic force microscopy (Supplementary Fig. 6) demonstrates spatially uniform current density with lower spatial variance than 2PACz.

### Mechanistic insights into perovskite crystallization dynamics and interfacial optimization

To elucidate SAM-dependent perovskite crystallization mechanisms, we conducted multimodal *in situ* monitoring combining photoluminescence (PL), ultraviolet-visible (UV-vis) absorption spectroscopy and X-ray diffraction (XRD) during thermal annealing. Supplementary Fig. 7 and Fig. 2a demonstrate that perovskite films on DMPP exhibit much more delayed PL intensity until stabilization (167.6 s) compared with 2PACz (49.5 s), corresponding to a much slower crystallization rate. It can also be observed that the stabilized PL intensity of the perovskite

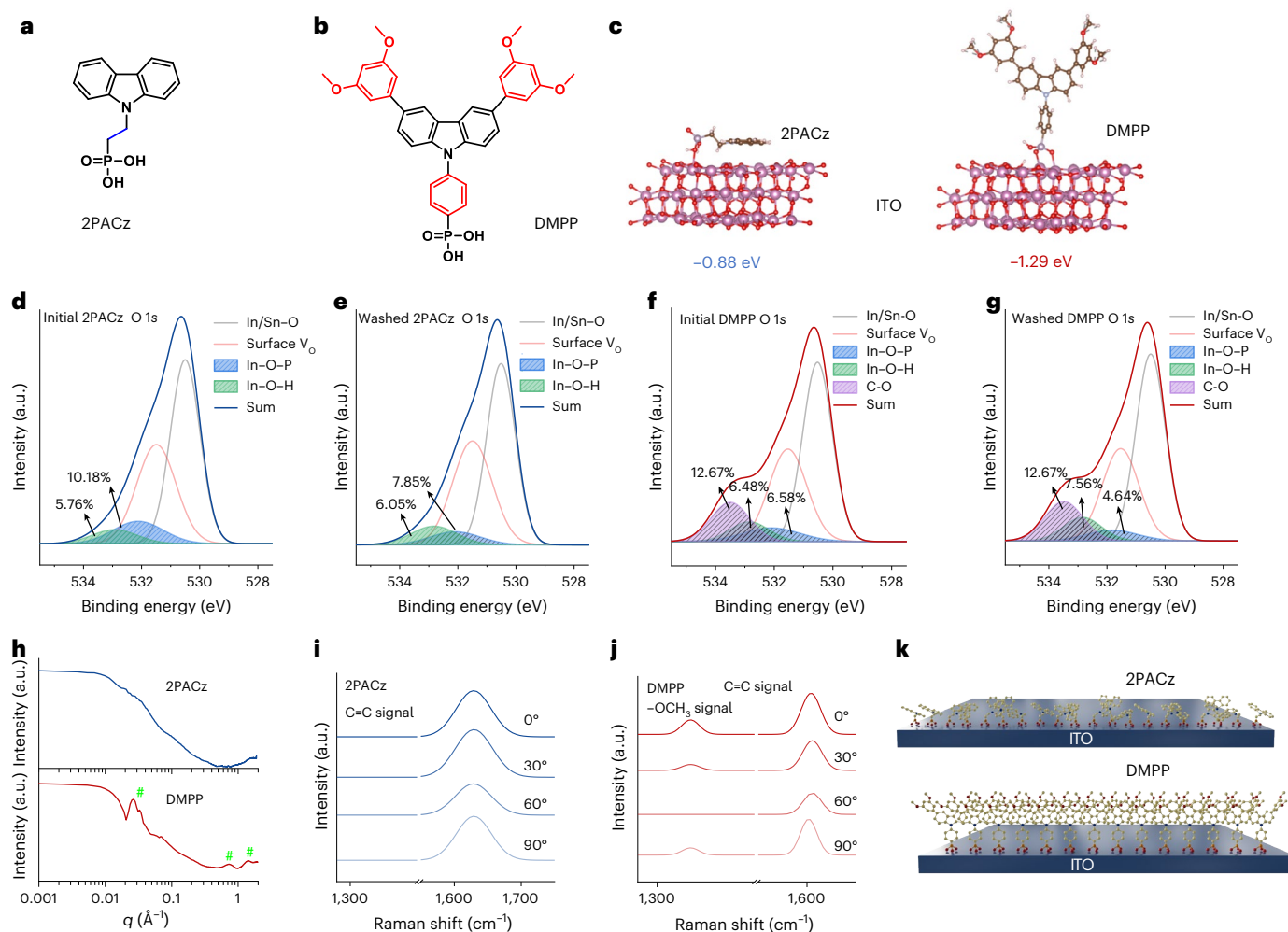


**Fig. 1 | Characterization of SAM properties.** **a, b**, Molecular structure of 2PACz (**a**) and DMPP (**b**). **c**, DFT-calculated binding configuration and energy of SAM and ITO. **d, e**, XPS analysis of the O1s chemical states in 2PACz before (**d**) and after (**e**) DMF cleaning. **f, g**, XPS analysis of the O1s chemical states in DMPP before (**f**) and

after (**g**) DMF cleaning. **h**, Grazing-incidence wide-angle X-ray scattering profiles of 2PACz and DMPP films on planar ITOs. **i, j**, Polarized Raman spectrum of 2PACz (**i**) and DMPP (**j**) films on planar ITOs. **k**, Structural schematic of 2PACz and DMPP molecules forming a film on planar ITOs.

film on DMPP is higher than that on 2PACz, indicative of better perovskite quality with less non-radiative recombination centres. Additionally, the PL half-width signal change of the perovskite film on 2PACz shows asymmetry, whereas the film on DMPP shows a much more symmetric change. This suggests better halide homogenization during perovskite crystallization on DMPP. This is corroborated by UV-vis phase evolution analysis (Supplementary Fig. 8). On 2PACz, a concurrent growth of the perovskite phase (738 nm) along with some other blend phases (more I rich or Br rich) indicates spatially heterogeneous crystallization. By contrast, DMPP substrates promote direct phase transformation with a single isosbestic point, suggesting homogeneous crystallization<sup>26</sup>.

Crucially, this crystallization disparity cannot be attributed to differences in substrate wettability. Contact angle measurements (Supplementary Fig. 9) showed only a marginal difference ( $\theta = 31.6^\circ$  for ITO/2PACz versus  $\theta = 33.6^\circ$  for ITO/DMPP,  $\Delta\theta \approx 2^\circ$ ), indicating that wettability is not the primary governing factor. The crystallization disparity instead originates from molecular-level interfacial interactions. XRD temporal profiles (Fig. 2b and Supplementary Fig. 10) that quantify crystallinity evolution show that the (100) peak intensity increases much slower with more orientation on DMPP than those on 2PACz, confirming enhanced crystallite alignment and perovskite phase transition<sup>34</sup>. As shown in Fig. 2c,d, this kinetic difference should stem from a differential precursor coordination. The ordered alignment of DMPP's  $-\text{OCH}_3$  groups, which preferentially coordinate

with Pb-related chemicals through Lewis acid–base interactions<sup>35</sup>, is revealed by Fourier transform infrared (FTIR) spectroscopy (Supplementary Fig. 11). This specific coordination modulates precursor supersaturation kinetics through two mechanisms: (1) reducing the effective concentration of Pb-related chemicals in precursor perovskite ink and (2) creating steric hindrance that delays final crystal formation, thereby delaying supersaturation attainment and enabling controlled crystallization. The reduction in effective concentration decreases the thermodynamic driving force for nucleation and, consequently, increases the nucleation work. Classical nucleation theory<sup>36</sup> dictates that the nucleation rate scales exponentially with the nucleation barrier (negative value). Therefore, the decreased driving force on DMPP significantly increases the nucleation work, suppressing perovskite nucleation. In situ optical microscopy during crystallization (Supplementary Fig. 12) directly validated that nucleation density was dramatically lower on DMPP compared with 2PACz, aligning with the predicted increase in the nucleation work. The resulting scarcity of nucleation sites along with the steric hindrance effect allows fewer crystals to dominate delayed growth, yielding larger perovskite grains with better crystallinity (Supplementary Figs. 13 and 14 shows the scanning electron microscopy (SEM) and XRD analyses).

Besides, residual stress analysis via XRD  $\sin^2\psi$  method<sup>37</sup> (Supplementary Fig. 15) provides critical mechanical insights that the perovskite film on DMPP exhibits almost no stress over the tensile

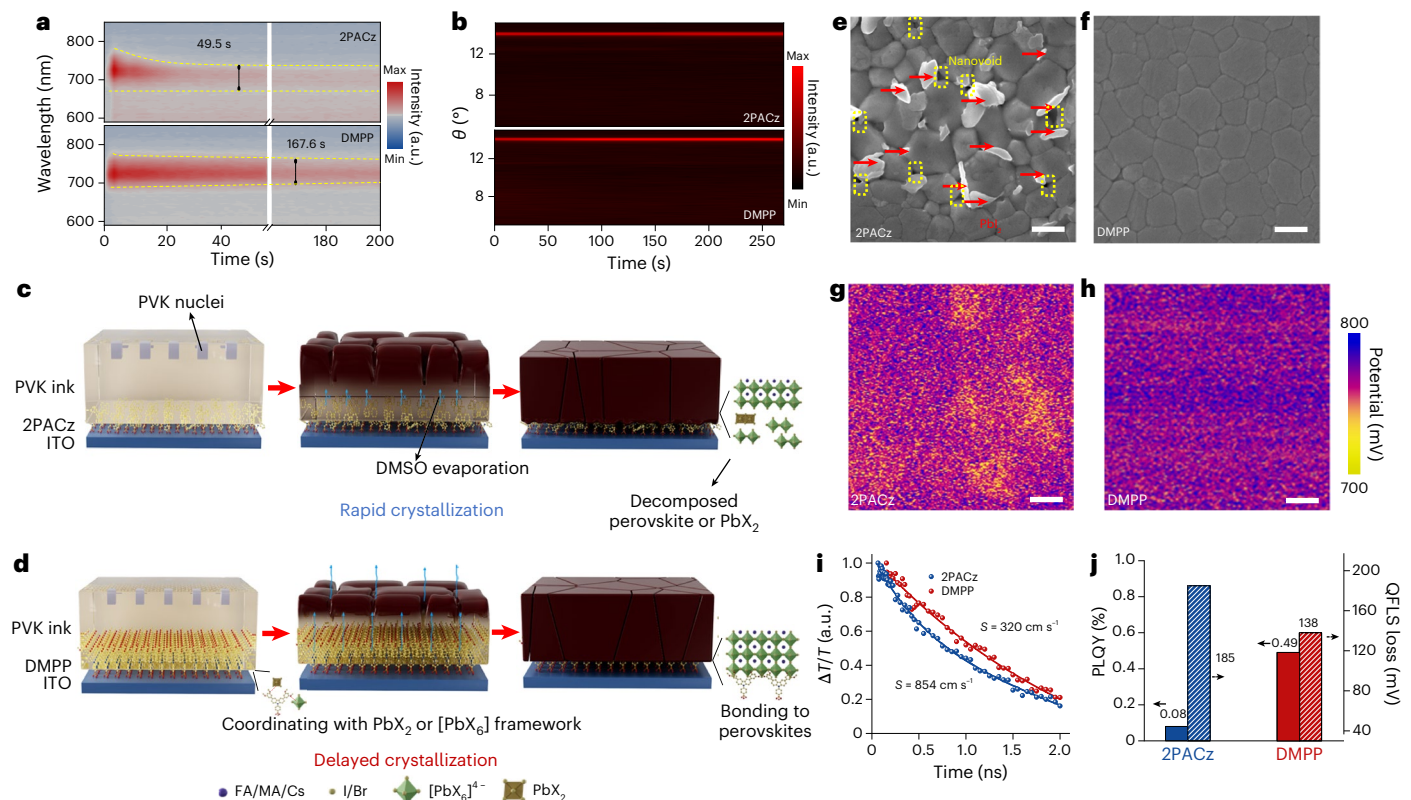


**Fig. 2 | Mechanism of SAM-regulated perovskite growth. a, b**, In situ PL (a) and XRD monitoring (b) of perovskite (PVK) crystallization on 2PACz and DMPP substrates. **c, d**, Schematic of the crystallization process of the perovskite film on 2PACz (c) and DMPP (d) substrates. **e, f**, SEM morphology of the buried surface after the perovskite films were peeled off from the 2PACz (e) and DMPP (f) substrates. Scale bars, 500 nm. **g, h**, KPFM potential distribution mapping of

the buried surface of the perovskite film on the 2PACz (g) and DMPP (h) substrates. Scale bars, 500 nm. **i**, Recombination rate of the SAM-perovskite buried interface obtained from the TAS test analysis. **j**, PLQY and quasi-Fermi-level splitting (QFLS) bar graphs of passivated perovskite films on 2PACz and DMPP substrates.

stressed one on 2PACz, attributed to improved lattice matching between the ordered SAM layer and the perovskite crystal structure. Delayed perovskite crystallization on DMPP allows complete DMSO evaporation, yielding pinhole-free buried perovskite surfaces with uniform grain packing compared with smaller perovskite grains with  $\text{PbI}_2$  segregations and nanovoids on 2PACz (Fig. 2e, f), induced by residual DMSO, which is evidenced by FTIR spectroscopy (Supplementary Fig. 16). This buried morphology improvement also correlates with atomic-force-microscopy-measured roughness reduction (Supplementary Fig. 17) due to the fact that the arranged DMPP film provides a more homogeneous substrate with stronger adsorption on perovskite surfaces ( $E_{\text{ads}} = -1.62$  eV versus  $-1.43$  eV for 2PACz; Supplementary Fig. 18), which would be better for interfacial charge transfer. Consequently, KPFM mappings demonstrate a reduction in surface potential fluctuation (Fig. 2g, h), confirming improved electronic homogeneity. The work functions were fitted to be 4.41 eV for the perovskite film on 2PACz and 4.37 eV for the film on DMPP through ultraviolet photoelectron spectroscopy (Supplementary Fig. 19), with the work-function difference aligning well with the trend observed in the KPFM results.

Next, we assessed the radiative properties of perovskite films by measuring their photoluminescence quantum yields (PLQYs; Fig. 2i), with the sample structure depicted in the insets. The perovskite film on DMPP exhibits a PLQY of 0.49%, approximately sixfold higher than that on 2PACz, suggesting a reduction in  $V_{\text{OC}}$  loss by about 47 mV in solar cell devices, as predicted by the quasi-Fermi-level splitting loss. We also utilized transient absorption spectroscopy (TAS; Fig. 2j and Supplementary Fig. 20) to quantify interfacial recombination dynamics<sup>38</sup>, showing over twofold longer carrier lifetime at DMPP-perovskite

interfaces. These enhancements might also correlate with defect passivation by the terminated group of DMPP, as revealed by obvious XPS-derived downshifts<sup>39</sup> of both Pb and I states for the buried perovskite surfaces (Supplementary Fig. 21). Feasible defects including neutral Pb interstitial ( $\text{Pb}_i^0$ ), positively charged I interstitial ( $\text{I}_i^+$ ) and positively charged undercoordinated  $\text{Pb}^{2+}$  (halide vacancy) passivated by DMPP are shown in Supplementary Fig. 22.

### Photoelectric properties of single-junction solar cells with DMPP

To characterize the electrical recombination properties of buried perovskite defects, we fabricated complete p-i-n single-junction perovskite solar cells (PSCs) with the architecture of ITO/SAMs/perovskite/piperazinium iodide (PI)/ $\text{C}_{60}$ /bathocuproine/Ag. The energetic profile of the trap density of states (tDOS) was measured and depicted in Fig. 3a and Supplementary Fig. 23. For PSCs utilizing 2PACz, the energy depth of tDOS was observed at approximately 0.3 eV. By contrast, PSCs incorporating DMPP exhibits a tDOS that was approximately 0.1 eV shallower. To further investigate the distribution of trap states across the devices, we conducted drive-level capacitance profiling (DLCP) measurements<sup>40</sup>. The results reveal that trap states at a depth of approximately 0.3 eV are predominantly located at the SAM-perovskite interface, and the introduction of DMPP reduces the density of these trap states significantly at the buried interfacial region (Fig. 3b and Supplementary Fig. 24). Through DFT calculations (Fig. 3c and Supplementary Fig. 25), we further assigned a 0.26-eV defect state below  $E_{\text{C}}$  to a  $\text{Pb}^0$  ( $\text{Pb}_i^0$ ) defect, and DMPP's electron-rich methoxy groups can passivate undercoordinated Pb via Lewis acid-base interactions. Besides, we calculated the energy level of interstitial  $\text{I}^+$  ( $\text{I}_i^+$ ) to locate

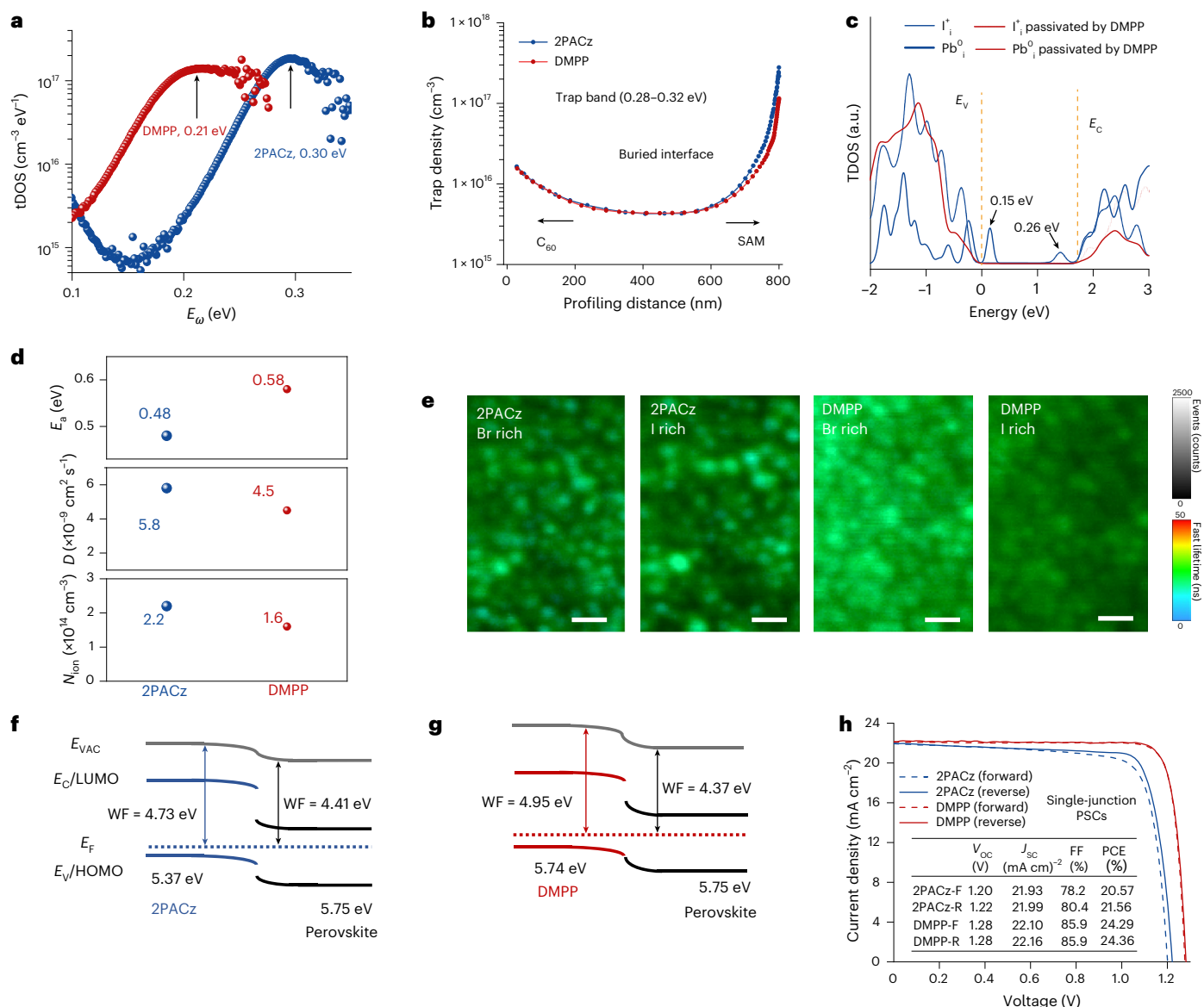


**Fig. 3 | Performance and optoelectronic characterization of PSCs. a, b**, tDOS (a) and DLCP (b) spectra of PSCs with 2PACz and DMPP. **c**, DFT calculations showing the defect energy level of the  $I_i^+$  and  $Pb_i^0$  defects, as well as the passivation of DMPP on defects. TDOS, total density of states. **d**,  $E_a$ ,  $D$  and  $N_{ion}$  extracted from the TID measurements representing ion migration in perovskites for PSCs with 2PACz and DMPP. **e**, Micro-area PL mapping phase

characterization of the peeled-off buried surface of perovskite films from 2PACz and DMPP substrates after 24 h of continuous light illumination. Scale bars, 1  $\mu$ m. **f, g**, Energy-level alignment at the 2PACz–perovskite (f) and DMPP–perovskite (g) interfaces. **h**,  $J$ – $V$  characteristics of the best-performing PSCs with 2PACz and DMPP. WF, work function.

0.15 eV above the  $E_v$ , finding that DMPP also successfully passivates this defect. It can be observed that DMPP reduces the interfacial trap density significantly, corroborating the DFT predictions of the total density of states within the bandgap. These findings correlate well with our previous experimental observations.

To assess the impact of the buried perovskite surface defects on ion migration within the perovskites, we used transient ion drift (TID) measurements<sup>41,42</sup>. This method effectively distinguishes between anion and cation migration. The transient capacitance indicates that the migrated ions are predominantly halide ions (Supplementary Fig. 26). Using the Arrhenius equation, we calculated the activation energy ( $E_a$ ) of halide ions to be 0.58 eV in PSCs with DMPP to be significantly higher than that to be 0.48 eV in PSCs with 2PACz, with the corresponding values for diffusion coefficient ( $D$ ) and mobile ion density ( $N_{ion}$ ) also demonstrating a marked reduction (Fig. 3d). This results in pronounced phase segregation in perovskites deposited

on 2PACz (Fig. 3e); pronounced signals of I-rich phases at wavelength exceeding 750 nm were observed in buried perovskites peeled off from 2PACz, whereas those from DMPP retain homogeneous halide distribution after 1-day light illumination. The formation of I-rich phases with narrowed bandgaps can adversely affect the  $V_{oc}$  of solar cell devices<sup>43</sup>. Additionally, the suppression of ion migration offers a significant enhancement in device long-term stability.

Given that the extended conjugation in DMPP, enhanced by the increased benzene rings, promotes molecular conductivity and facilitates more efficient hole extraction from perovskites to the DMPP layer, we conducted transient PL measurements to investigate interfacial carrier dynamics<sup>44</sup>. Following the deposition of perovskite layers with top-surface passivation on SAM substrates, both samples exhibit double-exponential PL decay profiles (Supplementary Fig. 27), reflecting enhanced carrier lifetimes in perovskites on DMPP. We extracted the diffusion time ( $\tau$ ) from PL decays (Supplementary Fig. 28).

The steepness of the  $t$  rise, influenced by charge transfer speed, is significantly greater for samples with DMPP compared with those with 2PACz.

To elucidate the energetic diagrams of these two interfaces, we utilized ultraviolet photoelectron spectroscopy measurements. As depicted in Supplementary Fig. 29, the work function of DMPP films is enhanced relative to 2PACz films. The energetics of the interfacial heterojunctions are illustrated in Fig. 3f,g, demonstrating an increased interfacial electric field and a reduced energy-level mismatch at the buried contacts of DMPP with perovskites. Consequently, under reverse scan, we achieved a peak PCE of 24.36% for PSCs using DMPP with minimal hysteresis compared with a forward PCE of 24.29%, primarily due to a significantly improved  $V_{oc}$  of 1.28 V and a fill factor (FF) of 85.9% (Fig. 3h). By contrast, PSCs utilizing 2PACz achieved a reverse PCE of only 21.56% with obvious hysteresis.

### Integration into tandem solar cells with silicon

We subsequently integrated the efficient perovskite top cells with DMPP onto a heterojunction silicon bottom cell, forming a monolithic tandem device, with the architecture illustrated in Fig. 4a. The perovskite grains are predominantly oriented vertically, effectively covering the textured silicon surface. As shown in Supplementary Fig. 30, we also detached perovskite films from silicon substrates. Examination of the buried surfaces revealed that films derived from 2PACz exhibit defective interfaces with prominent  $PbI_2$  flakes and nanovoids. By contrast, these morphological defects are significantly reduced in DMPP-derived films. These findings corroborate our observations on planar ITO substrates. Following optimization of the transparent top electrode and antireflection layers, the median photovoltaic values averaged over ten tandem devices indicate a PCE of 33.62%, a  $V_{oc}$  of 1.97 V, an FF of 83.01% and a short-circuit current density ( $J_{sc}$ ) of 20.47 mA cm<sup>-2</sup> with DMPP, compared with a PCE of 31.31%, a  $V_{oc}$  of 1.94 V, an FF of 79.07% and a  $J_{sc}$  of 20.45 mA cm<sup>-2</sup> with 2PACz (Fig. 4b). The observed improvements in  $V_{oc}$  and FF are probably attributable to the high performance of single-junction PSCs, which can be linked to reduced contact losses at the DMPP–perovskite interface. In particular,  $J_{sc}$  remains almost consistent, as evidenced by direct comparisons of external quantum efficiency (EQE) for representative tandem devices (Fig. 4c). The photogenerated  $J_{sc}$  values of 20.82 and 20.64 mA cm<sup>-2</sup> were obtained for the perovskite and silicon subcells in tandem with DMPP, respectively. With an improved  $V_{oc}$  of 1.98 V and an FF of 83.4%, the tandem achieves a champion PCE of 33.86% at reverse scan (33.76% at forward scan) with stabilized efficiency of 33.51%, compared with a reverse scan value of 31.65% (30.02% at forward scan) with stabilized 31.30% for the tandem with 2PACz (Fig. 4d,e). This tandem configuration has been sent to a third-party institution for certification, with the resulting PCE certified as 33.59% over a 0.979-cm<sup>2</sup> specified area with stabilized 33.03% efficiency (Supplementary Figs. 31 and 32). For a comprehensive comparison, we also fabricated tandem solar cells using the widely used SAMs, [4-(3,6-dimethyl-9H-carbazol-9-yl)butyl]phosphonic acid and [4-(3,6-dimethoxy-9H-carbazol-9-yl)butyl]phosphonic acid, with the best performance shown in Supplementary Fig. 33, which represent current high-performance standards<sup>4,6</sup>. The DMPP-based tandem cell significantly outperformed both [4-(3,6-dimethyl-9H-carbazol-9-yl)butyl]phosphonic acid (32.78%) and [4-(3,6-dimethoxy-9H-carbazol-9-yl)butyl]phosphonic acid (32.62%).

### Fig. 4 | Photovoltaic and stability performance of perovskite–silicon tandem solar cells.

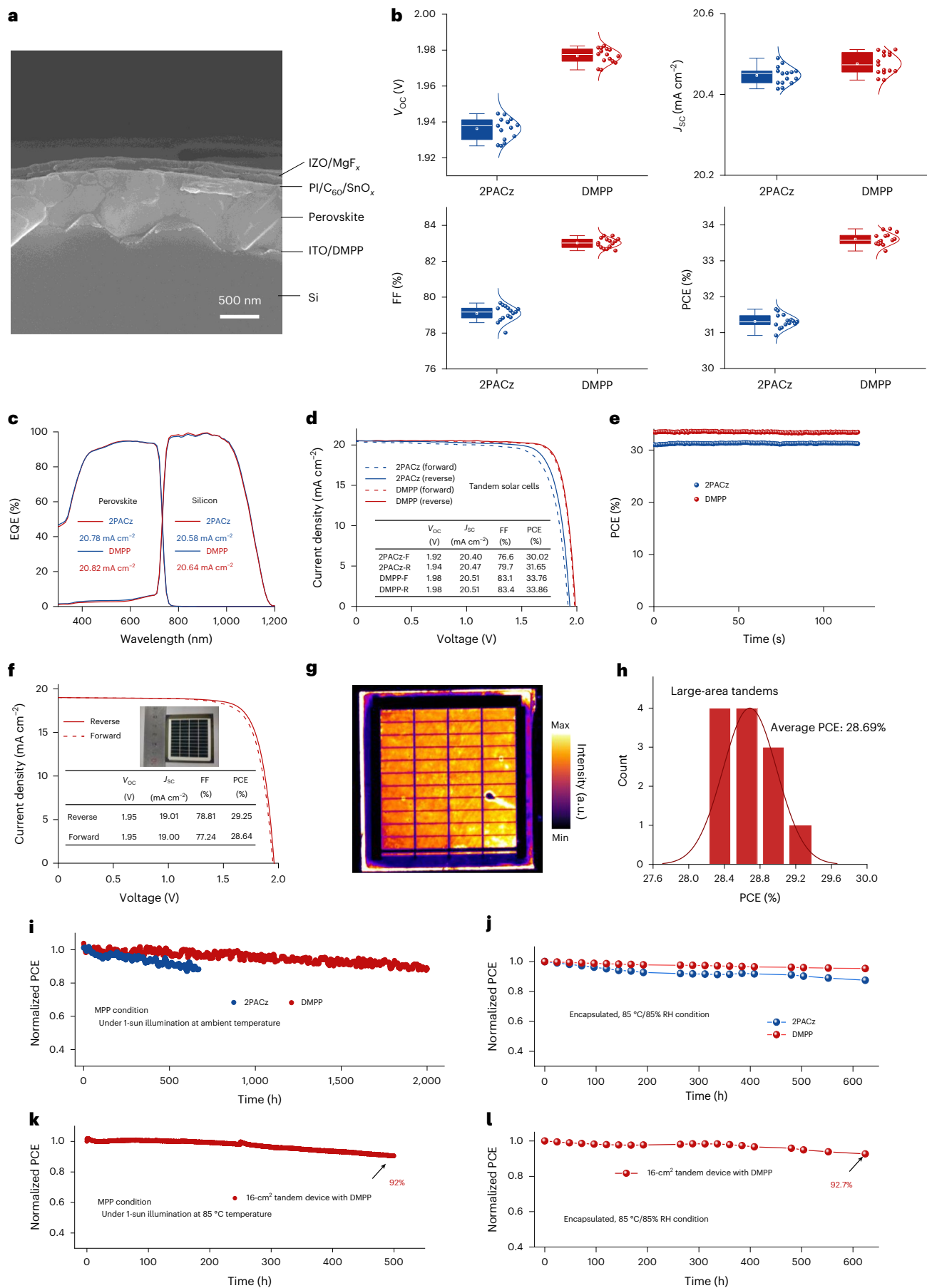
**a**, Cross-sectional SEM analysis of the perovskite–silicon tandem device. **b**, Statistical analysis of photovoltaic parameters including  $V_{oc}$ ,  $J_{sc}$ , FF and PCE. The box plots show the median (centre line), 25th to 75th percentiles (box bounds), minima to maxima (whiskers) and individual data points (circles). The data from  $n = 15$  independent devices per group are shown. **c**, EQE analysis and current matching of the typical tandem devices. **d**,  $J$ – $V$  characteristics of the champion perovskite–silicon tandem solar cells. **e**, Steady-state efficiency

To assess scalability, we fabricated tandem devices with an active area of 16-cm<sup>2</sup> active area (Fig. 4f, inset). Despite the increased device size, the champion device achieves a PCE of 29.25% (reverse scan:  $V_{oc} = 1.95$  V, FF = 78.81%,  $J_{sc} = 19.01$  mA cm<sup>-2</sup>), with a certified PCE of 28.53% and a stabilized efficiency of 28.39% (Supplementary Fig. 34). The minimal  $V_{oc}$  loss compared with small-area devices indicates good buried interfacial contacts (Fig. 4f). However,  $J_{sc}$  exhibits a noticeable decline, primarily due to increased shadowing effects from the Ag electrode grid, along with a reduction in FF caused by the transverse resistance loss of enlarged transparent electrode window layer affected by grid designs<sup>45</sup>, which consequently leads to a reduced overall PCE. The high PCE achieved can be attributed to the photoelectric uniformity of tandems devices, as evidenced by macro-PL mapping (Fig. 4g). Efficiency distribution analysis across ten large-area tandem devices (Fig. 4h) reveals an average PCE of 28.66%, confirming good reproducibility. The results highlight the effectiveness of DMPP interface engineering in achieving ordered molecular alignment for large-scale applications.

The optimized buried contacts, which effectively mitigate defects and ion migration in perovskites, allow us to evaluate the operational stability of these tandem solar cells. Under continuous 1-sun illumination in nitrogen at the MPP output, the device's surface temperature would rise to nearly 50 °C and stabilize after a day of continuous light exposure at room temperature. The 1-cm<sup>2</sup> unencapsulated DMPP-based tandem device retains >90% initial efficiency after 2,000 h, far exceeding the 2PACz-based tandem that retains <90% initial efficiency only after 700 h (Fig. 4i). Extended MPP tracking at elevated 85 °C further confirms DMPP's odds that the tandem demonstrates >90% PCE retention after 800 h compared with 73% for that with 2PACz. Specifically, we also conducted this test on the tandems with two other widely used SAMs, namely, [4-(3,6-dimethyl-9H-carbazol-9-yl)butyl]phosphonic acid and [4-(3,6-dimethoxy-9H-carbazol-9-yl)butyl]phosphonic acid<sup>4,6,46</sup>, and they demonstrate 81% and 83% PCE retentions after the same aging time, respectively, still inferior to the DMPP counterpart (Supplementary Fig. 35). Next, photothermal (85 °C/1-sun illumination) tests at open-circuit conditions reveal 90.8% retention (384 h) and 80.9% (624 h) for DMPP versus >50% loss for 2PACz (Supplementary Fig. 36). The more serious degradation stems from the inefficient charge carrier extraction at the two interfaces of the perovskite top cells compared with the bias-driven MPP tests. Cross-sectional SEM (Supplementary Fig. 37) of aged small-area devices validates these trends in which 2PACz-based tandems exhibit severe perovskite decomposition with voids and  $PbI_2$  flakes at buried interfaces, whereas DMPP-based devices show only minor localized degradation. Crucially, damp-heat testing (85 °C/85% relative humidity (RH); Fig. 4j) based on encapsulated tandem devices shows that the DMPP-based tandems retain 95.4% average PCE after 624 h versus 86.8% for the 2PACz-based tandems, indicating great damp-heat tolerance.

To underscore scalability, we conducted stability tests on 16-cm<sup>2</sup> tandem devices under continuous 1-sun illumination (85 °C, N<sub>2</sub> atmosphere; Fig. 4k). The results demonstrated 92% retention of initial efficiency after 500 h. Post-aging SEM analysis (Supplementary Fig. 38) reveals flake-like perovskite decomposition and small impurities in the cross-sectional view, suggesting a tendency towards degradation. Furthermore, in damp-heat tests (85 °C/85% RH; Fig. 4l), the typical large-area cell retained >92.7% of its initial PCE after 624 h, with only

of the tandem devices. **f**,  $J$ – $V$  characteristics of a 16-cm<sup>2</sup> tandem solar cell device with DMPP. **g**, Macro-PL mapping of the perovskite film deposited on 16-cm<sup>2</sup> DMPP-coated silicon substrate. **h**, PCE statistics of ten tandems in 16-cm<sup>2</sup> area with DMPP. **i**, Long-term operational stability of the tandem device. **j**, Damp-heat testing of 1-cm<sup>2</sup> tandem devices with 2PACz and DMPP at 85 °C/85% RH. **k**, MPP tracking of 16-cm<sup>2</sup> tandem device with DMPP at 85 °C. **l**, Damp-heat testing of 16-cm<sup>2</sup> tandem device with DMPP at 85 °C/85% RH.



a 7.3% relative drop. These results are comparable with small-area devices, confirming the robustness of the DMPP-modified interface at scale.

Beyond interfacial improvements, we investigated the intrinsic stability of DMPP and its spin-coated SAM layer on ITO. Photothermal stability tests (1-sun illumination, -65 °C, 48 h; Supplementary Fig. 39) using <sup>1</sup>H nuclear magnetic resonance in DMSO-*d*<sub>6</sub> reveals that 2PACz exhibited significant spectral changes, including new peaks at -11.3 ppm (carbazole N-H), indicating cleavage between the carbazole core and phosphate-linked alkyl chain. By contrast, DMPP shows unchanged spectra, confirming no core/linker cleavage, attributed to the benzene linker's enhanced stabilization of carbazole radicals. Additionally, we observed that DMPP exhibits enhanced molecular rigidity compared with 2PACz, as revealed by multiple cyclic voltammetry tests (Supplementary Fig. 40). This enhancement is probably attributed to the expanded  $\pi$ -conjugated system<sup>27</sup> in DMPP, which stabilizes the molecular structure through enhanced electron delocalization, thereby resisting redox-induced degradation. All these improvements contribute to the long-term stability of tandem devices with DMPP.

By redefining the role of SAMs in perovskite-silicon tandems, this work establishes a materials-by-design framework for interfacial optimization. The demonstrated efficiency and stability metrics position two-terminal tandems as a viable candidate for photovoltaics, accelerating the transition towards sustainable energy systems.

## Online content

Any methods, additional references, Nature Portfolio reporting summaries, source data, extended data, supplementary information, acknowledgements, peer review information; details of author contributions and competing interests; and statements of data and code availability are available at <https://doi.org/10.1038/s41566-025-01778-y>.

## References

- Eperon, G. E., Hörantner, M. T. & Snaith, H. J. Metal halide perovskite tandem and multiple-junction photovoltaics. *Nat. Rev. Chem.* **1**, 0095 (2017).
- Leijtens, T., Bush, K. A., Prasanna, R. & McGehee, M. D. Opportunities and challenges for tandem solar cells using metal halide perovskite semiconductors. *Nat. Energy* **3**, 828–838 (2018).
- Bush, K. A. et al. Thermal and environmental stability of semi-transparent perovskite solar cells for tandems enabled by a solution-processed nanoparticle buffer layer and sputtered ITO electrode. *Adv. Mater.* **28**, 3937–3943 (2016).
- Ugur, E. et al. Enhanced cation interaction in perovskites for efficient tandem solar cells with silicon. *Science* **385**, 533–538 (2024).
- Mariotti, S. et al. Interface engineering for high-performance, triple-halide perovskite-silicon tandem solar cells. *Science* **381**, 63–69 (2023).
- Liu, J. et al. Perovskite/silicon tandem solar cells with bilayer interface passivation. *Nature* **635**, 596–603 (2024).
- Qu, G. et al. Self-assembled materials with an ordered hydrophilic bilayer for high performance inverted perovskite solar cells. *Nat. Commun.* **16**, 86 (2025).
- He, R. et al. Improving interface quality for 1-cm<sup>2</sup> all-perovskite tandem solar cells. *Nature* **618**, 80–86 (2023).
- Li, C. et al. Pros and cons of hole-selective self-assembled monolayers in inverted PSCs and TSCs: extensive case studies and data analysis. *Energy Environ. Sci.* **17**, 6157–6203 (2024).
- Li, Z. et al. Stabilized hole-selective layer for high-performance inverted p-i-n perovskite solar cells. *Science* **382**, 284–289 (2023).
- Zhu, J. et al. A donor-acceptor-type hole-selective contact reducing non-radiative recombination losses in both subcells towards efficient all-perovskite tandems. *Nat. Energy* **8**, 714–724 (2023).
- Zhumagali, S. et al. Efficient narrow bandgap Pb-Sn perovskite solar cells through self-assembled hole transport layer with ionic head. *Adv. Energy Mater.* **15**, 2404617 (2025).
- Zhang, S. et al. Minimizing buried interfacial defects for efficient inverted perovskite solar cells. *Science* **380**, 404–409 (2023).
- Zhou, J. et al. Molecular contacts with an orthogonal  $\pi$ -skeleton induce amorphization to enhance perovskite solar cell performance. *Nat. Chem.* **17**, 564–570 (2025).
- Wang, X. et al. Regulating phase homogeneity by self-assembled molecules for enhanced efficiency and stability of inverted perovskite solar cells. *Nat. Photon.* **18**, 1269–1275 (2024).
- Shi, C. et al. Modulating competitive adsorption of hybrid self-assembled molecules for efficient wide-bandgap perovskite solar cells and tandems. *Nat. Commun.* **16**, 3029 (2025).
- Chen, S. et al. Stabilizing perovskite-substrate interfaces for high-performance perovskite modules. *Science* **373**, 902–907 (2021).
- Chin, X. Y. et al. Interface passivation for 31.25%-efficient perovskite/silicon tandem solar cells. *Science* **381**, 59–63 (2023).
- Er-raji, O. et al. Tailoring perovskite crystallization and interfacial passivation in efficient, fully textured perovskite silicon tandem solar cells. *Joule* **8**, 2811–2833 (2024).
- Tong, X. et al. Large orientation angle buried substrate enables efficient flexible perovskite solar cells and modules. *Adv. Mater.* **36**, 2407032 (2024).
- Park, S. M. et al. Low-loss contacts on textured substrates for inverted perovskite solar cells. *Nature* **624**, 289–294 (2023).
- Zhang, X. et al. Reinforcing coverage of self-assembled monomolecular layers for inverted perovskite solar cells with efficiency of 25.70%. *Angew. Chem. Int. Ed.* **64**, e202423827 (2025).
- Kan, C. et al. Efficient and stable perovskite-silicon tandem solar cells with copper thiocyanate-embedded perovskite on textured silicon. *Nat. Photon.* **19**, 63–70 (2025).
- Chen, S. et al. Crystallization in one-step solution deposition of perovskite films: upward or downward?. *Sci. Adv.* **7**, eabb2412 (2021).
- Fang, Z., Nie, T., Liu, S. F. & Ding, J. Overcoming phase segregation in wide-bandgap perovskites: from progress to perspective. *Adv. Funct. Mater.* **34**, 2404402 (2024).
- Wang, R. et al. Efficient wide-bandgap perovskite photovoltaics with homogeneous halogen-phase distribution. *Nat. Commun.* **15**, 8899 (2024).
- Dong, B. et al. Self-assembled bilayer for perovskite solar cells with improved tolerance against thermal stresses. *Nat. Energy* **10**, 342–353 (2025).
- Zhao, K. et al. *peri*-Fused polyaromatic molecular contacts for perovskite solar cells. *Nature* **632**, 301–306 (2024).
- Tang, H. et al. Reinforcing self-assembly of hole transport molecules for stable inverted perovskite solar cells. *Science* **383**, 1236–1240 (2024).
- Jiang, W. et al. Spin-coated and vacuum-processed hole-extracting self-assembled multilayers with H-aggregation for high-performance inverted perovskite solar cells. *Angew. Chem. Int. Ed.* **63**, e202411730 (2024).
- Aydin, E. et al. Enhanced optoelectronic coupling for perovskite/silicon tandem solar cells. *Nature* **623**, 732–738 (2023).
- Darabi, K. et al. Cationic ligation guides quantum-well formation in layered hybrid perovskites. *Matter* **7**, 4410–4425 (2024).
- Qin, W. et al. Suppressing non-radiative recombination in metal halide perovskite solar cells by synergistic effect of ferroelasticity. *Nat. Commun.* **14**, 256 (2023).
- Sidhik, S. et al. Two-dimensional perovskite templates for durable, efficient formamidinium perovskite solar cells. *Science* **384**, 1227–1235 (2024).

35. Lee, J.-W., Kim, H.-S. & Park, N.-G. Lewis acid–base adduct approach for high efficiency perovskite solar cells. *Acc. Chem. Res.* **49**, 311–319 (2016).
36. Gebauer, D., Kellermeier, M., Gale, J. D., Bergström, L. & Cölfen, H. Pre-nucleation clusters as solute precursors in crystallisation. *Chem. Soc. Rev.* **43**, 2348–2371 (2014).
37. Hang, P. et al. Highly efficient and stable wide-bandgap perovskite solar cells via strain management. *Adv. Funct. Mater.* **33**, 2214381 (2023).
38. Zhang, D. et al. Mitigated front contact energy barrier for efficient and stable perovskite solar cells. *Energy Environ. Sci.* **17**, 3848–3854 (2024).
39. Cheng, M. et al. Tailoring buried interface and minimizing energy loss enable efficient narrow and wide bandgap inverted perovskite solar cells by aluminum glycinate based organometallic molecule. *Adv. Mater.* **37**, 2419413 (2025).
40. Ni, Z. et al. Resolving spatial and energetic distributions of trap states in metal halide perovskite solar cells. *Science* **367**, 1352–1358 (2020).
41. Yao, Y. et al. Oriented wide-bandgap perovskites for monolithic silicon-based tandems with over 1,000 hours operational stability. *Nat. Commun.* **16**, 40 (2025).
42. Li, B. et al. Promising excitonic absorption for efficient perovskite solar cells. *Joule* **9**, 101780 (2025).
43. Datta, K. et al. Effect of light-induced halide segregation on the performance of mixed-halide perovskite solar cells. *ACS Appl. Energy Mater.* **4**, 6650–6658 (2021).
44. Al-Ashouri, A. et al. Monolithic perovskite/silicon tandem solar cell with >29% efficiency by enhanced hole extraction. *Science* **370**, 1300–1309 (2020).
45. Rehman, A. U. et al. Electrode metallization for scaled perovskite/silicon tandem solar cells: challenges and opportunities. *Prog. Photovolt.* **31**, 429–442 (2023).
46. Subbiah, A. S. et al. Efficient blade-coated perovskite/silicon tandems via interface engineering. *Joule* **9**, 101767 (2025).

**Publisher's note** Springer Nature remains neutral with regard to jurisdictional claims in published maps and institutional affiliations.

Springer Nature or its licensor (e.g. a society or other partner) holds exclusive rights to this article under a publishing agreement with the author(s) or other rightsholder(s); author self-archiving of the accepted manuscript version of this article is solely governed by the terms of such publishing agreement and applicable law.

© The Author(s), under exclusive licence to Springer Nature Limited 2025

## Methods

### Materials

All chemicals were used as received.  $\text{PbI}_2$  (99.99%), caesium iodide (99.99%) and 2PACz were purchased from TCI. Formamidinium iodide (99.9%), methylammonium bromide (99.5%), lead bromide (99.99%), PI and  $\text{C}_{60}$  (>99.9% purity) were purchased from Xi'an Yuri Solar. Zinc-doped indium oxide ( $\text{In}_2\text{O}_3/\text{ZnO}$ : 90/10 wt%, 99.99%) were purchased from ZhongNuo Advanced Material Technology. Magnesium fluoride (99.99%) was purchased from Hebei Luohong Technology. Tetrakis(dimethylamino) tin(IV) (99.99%) as one precursor of  $\text{SnO}_2$  was purchased from Nanjing Ai Mou Yuan Scientific Equipment. Ethanol was purchased from Shanghai Aladdin Biochemical Technology. DMF (anhydrous, 99.9%), DMSO (anhydrous, >99.9%), chlorobenzene (anhydrous, 99.9%) and isopropanol (anhydrous, 99.9%) were purchased from Sigma-Aldrich. DMPP was obtained synthetically, and the details are described in Supplementary Text 1.

### Perovskite single-junction preparation

The  $15 \times 15\text{-mm}^2$  ITO glass substrates were sequentially sonicated in deionized water, ethanol, acetone and isopropanol for 5 min each. Following sonication, the substrates were dried using a hot-air blower and subjected to UV–ozone treatment for 15 min. Subsequently, the substrates were transferred into a nitrogen-filled glovebox. SAMs were prepared using  $1 \text{ mg ml}^{-1}$  of 2PACz solutions in ethanol and DMPP in methanol. These solutions were spin coated onto the substrates at 5,000 rpm for 30 s, followed by annealing at  $100^\circ\text{C}$  for 10 min. The 1.4-M perovskite  $\text{Cs}_{0.05}\text{FA}_{0.8}\text{MA}_{0.15}\text{Pb}(\text{I}_{0.75}\text{Br}_{0.25})_3$  precursor solution, with a bandgap of 1.68 eV, was prepared by dissolving a mixture of formamidinium iodide, methylammonium bromide,  $\text{PbI}_2$ , lead bromide and caesium iodide in a 4:1 (vol/vol) mixture of anhydrous DMF and DMSO. A  $50 \mu\text{l}$  of the precursor solution was spin coated onto the substrates at 1,000 rpm for 10 s, followed by 1,000 rpm for 10 s and 5,000 rpm for 40 s. During the spin-coating process,  $150 \mu\text{l}$  of chlorobenzene was dropped onto the film 10 s before the completion of spinning. The resulting perovskite film was immediately annealed at  $100^\circ\text{C}$  for 15 min. Subsequently, a  $0.4 \text{ mg ml}^{-1}$  of PI solution in isopropanol was spin coated onto the perovskite films at 5,000 rpm for 30 s and annealed at  $100^\circ\text{C}$  for 10 min. Finally, 20 nm of  $\text{C}_{60}$ , 5 nm of bathocuproine and 100 nm of Ag were thermally evaporated onto the perovskite film at deposition rates of  $0.2 \text{ \AA s}^{-1}$ ,  $0.1 \text{ \AA s}^{-1}$  and  $1 \text{ \AA s}^{-1}$ , respectively.

### Silicon heterojunction bottom-cell fabrication

N-type Czochralski silicon wafers with a resistivity of 1–2  $\Omega \text{ cm}$  and a thickness of 150  $\mu\text{m}$  were used to fabricate the silicon bottom cell. An initial etching step was performed to remove surface saw damage, followed by a standard texturing process to create a double-sided random pyramid texture. This process resulted in an average pyramid height of less than 1.5  $\mu\text{m}$  on both sides. After undergoing a standard RCA cleaning process, the wafers were dipped in a buffered HF solution. The samples were then transferred to a plasma-enhanced chemical vapour deposition cluster for the deposition of surface passivation stacks. Hydrogenated intrinsic amorphous silicon (i-a-Si:H) layers with thicknesses of approximately 5 nm and 9 nm were deposited on the front and rear sides of the textured wafers, respectively. On the front side, an n-type nanocrystalline silicon oxide (nc-SiO<sub>2</sub>:H) layer with a thickness of approximately 15 nm was deposited, whereas a p-type nanocrystalline silicon (nc-Si:H) layer of about 12 nm was deposited on the rear side. To complete the silicon bottom-cell fabrication, a 15-nm-thick transparent conductive oxide layer was deposited on the front side, and a 75-nm-thick transparent conductive oxide layer was deposited on the rear side, followed by Ag screen printing. The front and rear transparent conductive oxide layers covered an area of  $1.08 \times 1.08 \text{ cm}^2$ . The silicon bottom cells were then laser cut into  $2.50 \times 2.50 \text{ cm}^2$  square substrates for tandem fabrication.

### Perovskite top-cell fabrication

The silicon bottom cells were cleaned under UV–ozone for 10 min and subsequently transferred to a nitrogen-filled glovebox. SAMs were prepared using  $1 \text{ mg ml}^{-1}$  of 2PACz solutions in ethanol and DMPP in methanol. These solutions were spin coated onto the silicon bottom cells at 5,000 rpm for 30 s, followed by annealing at  $100^\circ\text{C}$  for 10 min. A 1.7-M perovskite precursor solution with a bandgap of 1.68 eV, composed of  $\text{Cs}_{0.05}\text{FA}_{0.8}\text{MA}_{0.15}\text{Pb}(\text{I}_{0.75}\text{Br}_{0.25})_3$ , was prepared by dissolving a mixture of formamidinium iodide, methylammonium bromide,  $\text{PbI}_2$ , lead bromide and caesium iodide in an anhydrous DMF:DMSO (4:1 vol/vol) solvent system. Then,  $100 \mu\text{l}$  of the precursor solution was spin coated onto the substrates at 2,500 rpm for 30 s, followed by 7,000 rpm for 10 s. During the spin-coating process,  $250 \mu\text{l}$  of chlorobenzene was dropped onto the film 10 s before the completion of spinning. The resulting perovskite film was immediately annealed at  $100^\circ\text{C}$  for 15 min. Subsequently, a  $0.4 \text{ mg ml}^{-1}$  of PI solution in isopropanol was spin coated onto the perovskite films at 5,000 rpm for 30 s, followed by annealing at  $100^\circ\text{C}$  for 10 min. A 15-nm-thick  $\text{C}_{60}$  layer was then thermally evaporated onto the perovskite film at a deposition rate of  $0.2 \text{ \AA s}^{-1}$ . A buffer layer of approximately 12 nm of  $\text{SnO}_2$  was deposited on the  $\text{C}_{60}$  layer using atomic layer deposition in a PE ALD-F50R (KE-MICRO) system at  $90^\circ\text{C}$ . The deposition process consisted of 100 cycles of using a tetrakis(dimethylamino) tin(IV) precursor ( $80^\circ\text{C}$ , 90 s.c.c.m., 1-s pulse, 6.0-s purge) and  $\text{H}_2\text{O}$  (90 s.c.c.m., 1-s pulse, 6.0-s purge). Zinc-doped indium oxide was subsequently sputtered onto the  $\text{SnO}_2$  layer through a shadow mask, achieving a sheet resistance of  $140 \Omega \square^{-1}$  and a thickness of 40 nm on flat glass. Finally, a 500-nm-thick Ag electrode and a 110-nm-thick magnesium fluoride layer were thermally evaporated at deposition rates of  $1 \text{ \AA s}^{-1}$  under a high vacuum. The  $16\text{-cm}^2$  tandem device was fabricated using  $5 \times 5\text{-cm}^2$  silicon substrates. The primary adjustment of the SAM and perovskite layer fabrication lies in scaling the volume of the precursor solution proportionally to the substrate size, ensuring uniform deposition across the larger active area. Here 20 nm of  $\text{C}_{60}$  followed by 10 nm of  $\text{SnO}_2$  and 40 nm of zinc-doped indium oxide were used. Both front and rear electrodes were prepared by the screen printing of Ag paste.

### DFT calculations

For the calculation of molecular properties, all the DFT calculations were performed using Gaussian16C.01 and the geometry optimization of SAMs was carried out at the B3LYP level using the 6-31G(d) basis set. Grimme's D3 (BJ) dispersion correction was applied to all the calculations. Assessing vibrational frequencies at the same level validates that the optimized structures correspond to true minima on their respective potential energy surfaces.

We used the DFT as implemented in the Vienna ab initio simulation package in all the calculations. The exchange–correlation potential was described by using the generalized gradient approximation of Perdew–Burke–Ernzerhof. The projector-augmented wave method and pseudopotentials were used to treat interactions between ion cores and valence electrons. We also used the Perdew–Burke–Ernzerhof generalized gradient approximation to describe electron–electron interactions. The surface was cleaved, a  $14 \text{ \AA}$  vacuum layer was added, and the bottom three layers were fixed for further structural optimization. The plane-wave cut-off energy was fixed to 450 eV. Given that the structural models were relaxed until the Hellmann–Feynman forces smaller than  $-0.02 \text{ eV \AA}^{-1}$  and the change in energy smaller than  $10^{-5} \text{ eV}$  was attained, the  $\Gamma$  point  $k$ -point sampling was used for the Brillouin-zone integration.

### Characterization

**Structural and optical analyses.** The XRD patterns of the perovskite were acquired using a D8 Discover X-ray diffractometer (Bruker) equipped with Cu K $\alpha$  radiation. To investigate the out-of-plane and in-plane crystallographic orientations, grazing-incidence wide-angle

X-ray scattering measurements were performed using a Xeuss 3.0 at the Vacuum Interconnected Nanotech Workstation (Nano-X) with a monochromatic Cu K $\alpha$  source and a detector (Eiger2 R 1M). The distance between the sample and the detector is 120 mm. The incident angle was set to 0.2° to probe the surface-sensitive structural features and crystallite alignment. The morphology of the perovskite was observed using a Hitachi S4800 (Hitachi) field-emission SEM instrument. For molecular orientation and vibrational mode analysis, polarized Raman spectroscopy was conducted using a Renishaw inVia Raman microscope equipped with a 532-nm laser. The deflection direction of the incident laser is set to four angles: 0°, 30°, 60° and 90°. Ultraviolet photoelectron spectroscopy measurements were carried out on a Thermo Fisher ESCALAB system with a monochromatic He I light (21.22 eV) as the excitation source. XPS characterization was performed using a Kratos AXIS Supra XPS device with monochromatic Al K $\alpha$  X-rays (1,486.6 eV). Transient PL measurements were conducted using an FLS1000 PL spectrometer, equipped with a 475-nm diode laser and a 600-nm longpass filter. Emission spectra were collected for wavelengths ranging from 600 nm to 850 nm. Additionally, TAS was performed using a femtosecond pump–probe system (HELIOS, Ultrafast Systems) to investigate the charge carrier dynamics and recombination processes in the perovskite materials. To monitor real-time changes in the optical and structural properties, in situ PL, UV–vis absorption and XRD measurements were conducted using customized setups. For in situ PL, a continuous-wave laser (405 nm) was used to excite the sample and monitor the emission intensity under controlled temperature and humidity conditions. In situ absorption studies were performed using a UV–vis–near-infrared spectrometer (LAMBDA 950, PerkinElmer) equipped with a temperature-controlled stage. In situ XRD measurements were carried out using a Bruker D8 Advance diffractometer with a heating stage to study structural evolution under a fixed temperature.

For phase separation analysis, micro-area PL mapping was performed using a confocal laser scanning microscope (PicoQuant Micro-Time 100 confocal microscopic system) with a 640-nm excitation laser. The spatial distribution of PL intensity was mapped across the sample surface to identify phase segregation and heterogeneities. To distinguish Br-rich and I-rich phases, we used a beamsplitter to separate the overall PL signal and simultaneously collected the two PL signals through 740-nm and 780-nm bandpass filters, which allow the spatial discrimination of Br-rich and I-rich perovskite phases, respectively. Macro-area PL mapping is executed by a laser scanning confocal microscope (WITec RAS300) equipped with a 473-nm pulse laser and galvo-based scanner. Finally, FTIR spectroscopy was conducted using a Thermo Scientific Nicolet iS10 spectrometer to analyse the molecular vibrations and chemical bonding in the perovskite material. The spectra were collected in the range of 4,000–400 cm<sup>-1</sup>.

**Electrical and surface measurements.** Contact potential and surface work function were analysed via KPFM (Bruker Dimension Icon). KPFM measurements were performed in the peak force tapping mode on a the Bruker Dimension Icon using scm-pit-v2 probes (0.01–0.025  $\Omega$  cm, antimony (n)-doped Si). The measurements were performed under AM-KPFM with 75-kHz resonant frequency, spring constant of 3.0 N m<sup>-1</sup> and 25-nm tip radius. Current density–voltage ( $J$ – $V$ ) curves were acquired under AM1.5 G illumination (Newport solar simulator, 94022A) using a Keithley 2400 source measure unit. The EQE was measured (PV Measurements QEX10) with wavelength-specific bias lighting. Capacitance, TAS and transient ion drift (TID) measurements were performed using a Keysight E4980A LCR meter. Capacitance–voltage measurements were conducted with an a.c. voltage of 20 mV at a frequency of 10 kHz. TAS measurements were performed under a d.c. bias of 0 V (unless otherwise specified) and an a.c. voltage of 20 mV, with a frequency scan ranging from 20 Hz to 1 MHz. TID measurements were carried out with a d.c. voltage of 0.9 V and an a.c. voltage of 20 mV

at a frequency of 10 kHz. For detailed steps and formulas, please refer to refs. 25,27.

The standard DLCP measurements were performed by using a Keysight E4980A precision LCR meter. In the DLCP measurement, the d.c. bias was scanned from 0 V to the  $V_{oc}$  (for example, 1.1 V) for the PSC. The DLCP method uses a series of variable  $\delta V$  (20 mV) to measure the junction capacitance and acquire the capacitance contribution from the trap states by taking advantage of the information embedded in the higher-order terms. The capacitance measured at each  $\delta V$  was recorded and fitted with a polynomial function to obtain  $C_0$  and  $C_1$ .

$$C = C_0 + C_1\delta V + C_2(\delta V)^2 \dots$$

With the determination of  $C_0$  and  $C_1$ , the carrier density ( $N$ ) that includes both free carrier density ( $N_0$ ) and trap density ( $N_T$ ) at a certain position  $X$  from the junction barrier is calculated by

$$N = -\frac{C_0^3}{2q\epsilon A^2 C_1},$$

where  $q$  is the elementary charge,  $\epsilon$  is the dielectric constant of the semiconductor and  $A$  is the active area of the junction. The profiling distance from the junction barrier was calculated by  $\epsilon A/C_0$ . For the comparison of trap densities, the trap densities measured at 10 kHz are representatively given in this work, which would not affect the comparison of the relative values as the trap densities are basically on the same order of magnitude with the change in a.c. frequency in the vicinity of 10 kHz. For detailed steps and formulas, please refer to ref. 28.

**Stability testing.** Encapsulated devices underwent MPP tracking under continuous 1-sun illumination (EnliTech SS-F5-3A) at various temperatures. For tandem encapsulation, the tandem devices were packaged using thermoplastic polyolefin films supplied by Baijia Times, applied via a lamination process. The encapsulation protocol involved heating to 130 °C under vacuum, with a stepwise pressure application: an initial vacuum of –20 kPa for 2 min, followed by –50 kPa for 3 min and a final pressure of –80 kPa for 5 min. This graded-pressure sequence ensures effective adhesion and minimizes mechanical stress on the device layers. The selected thermoplastic polyolefin material offers robust moisture and oxygen barrier properties, critical for long-term device stability.

### Data acquisition

For single-junction PSCs,  $J$ – $V$  measurements were conducted in both reverse scan (1.3 V to –0.1 V, step size of 0.013 V, with a dwelling time of 10 ms per step) and forward scan (–0.1 V to 1.3 V, step size of 0.013 V, with a dwelling time of 10 ms per step). The device was tested using a calibrated mask with an aperture area of 0.0568 cm<sup>2</sup>.

For perovskite–silicon tandem solar cells,  $J$ – $V$  curves were measured in both reverse scan (2.0 V to –0.1 V, step size of 0.013 V, with a dwelling time of 10 ms per step) and forward scan (–0.1 V to 2.0 V, step size of 0.013 V, with a dwelling time of 10 ms per step). The device was tested with a calibrated mask having an aperture area of 1 cm<sup>2</sup>.

All the measurements were conducted at room temperature (25  $\pm$  5 °C) and relative humidity of 30  $\pm$  10% under ambient conditions. No preconditioning, such as light soaking, was applied before measurements. The steady-state PCE was determined by measuring the stabilized photocurrent density under a constant bias voltage. Spectral mismatch was corrected using a KG5-filtered Si reference cell.

EQE spectra were recorded using an EQE measurement system (model QEX10, PV Measurements) with a chopped monochromatic light beam fully focused on the active area of the tandem cells. For the perovskite top-cell measurement, the silicon bottom cells were saturated using an infrared-light-bias light-emitted diode with a peak emission at 850 nm. A bias voltage of 0.6 V was applied to approximate

short-circuit conditions. For silicon bottom-cell measurements, a blue-light-bias light-emitted diode with a peak emission at 455 nm was used to saturate the perovskite subcells, and a 1-V bias voltage was applied to maintain short-circuit conditions.

### Reporting summary

Further information on research design is available in the Nature Portfolio Reporting Summary linked to this article.

### Data availability

The main data supporting the findings of this study are available in the article and the Supplementary Information. All other data related to this work are available from the corresponding authors on request. Source data are provided with this paper.

### Acknowledgements

X.Y. acknowledges grants by the National Natural Science Foundation of China (U23A20354 and 62025403), National Key Research and Development Program of China (2023YFB4202504), the Baima Lake Laboratory Joint Funds of the Zhejiang Provincial Natural Science Foundation of China (LBMHD24E020002) and ‘Pioneer’ and ‘Leading Goose’ R&D Program of Zhejiang (2024C01092). M.L. acknowledges funding support from the National Natural Science Foundation of China (21975219). P.H. acknowledges funding support from the National Natural Science Foundation of China (62304201) and ‘Pioneer’ and ‘Leading Goose’ R&D Program of Zhejiang (2025C01154).

### Author contributions

D.Z., B.Y. and P.H. conceived the idea, designed the experiments and wrote the original draft. B.Y. contributed to DMPP’s synthesis and

structural characterization. D.Z. fabricated the devices and conducted the  $J$ - $V$ , EQE, SEM, PL, XPS, XRD and stability measurements. D.Z. and R.X. contributed to the device fabrication and certification. R.X. and Y.C. contributed to the extra tandem certification in ESTI. D.Z. and H.Z. contributed to the PL mapping measurements. H.X. and Z.N. contributed to the DLCP measurements and related analysis. R.L. and B.L. contributed to the TAS and TID tests. J.W. assisted in the in situ characterizations and data processing. R.X. and J.G. designed and prepared the silicon bottom cells. X.Y., M.L. and P.H. provided funding support. X.Y., M.L. and P.H. revised the paper. P.H., X.Y., M.L., J.G. and D.Y. supervised the experimental development, led the project and reviewed the paper. All authors discussed the results and commented on the paper.

### Competing interests

The authors declare no competing interests.

### Additional information

**Supplementary information** The online version contains supplementary material available at <https://doi.org/10.1038/s41566-025-01778-y>.

**Correspondence and requests for materials** should be addressed to Pengjie Hang, Ming Lei, Jifan Gao, Deren Yang or Xuegong Yu.

**Peer review information** *Nature Photonics* thanks Zhaoning Song and the other, anonymous, reviewer(s) for their contribution to the peer review of this work.

**Reprints and permissions information** is available at [www.nature.com/reprints](http://www.nature.com/reprints).

## Solar Cells Reporting Summary

Nature Portfolio wishes to improve the reproducibility of the work that we publish. This form is intended for publication with all accepted papers reporting the characterization of photovoltaic devices and provides structure for consistency and transparency in reporting. Some list items might not apply to an individual manuscript, but all fields must be completed for clarity.

For further information on Nature Research policies, including our [data availability policy](#), see [Authors & Referees](#).

### ► Experimental design

Please check the following details are reported in the manuscript, and provide a brief description or explanation where applicable.

#### 1. Dimensions

Area of the tested solar cells	<input checked="" type="checkbox"/> Yes <input type="checkbox"/> No	<div style="border: 1px solid #ccc; padding: 2px; margin-bottom: 2px;">The active area of the device is 0.9793 cm<sup>2</sup> and 16.164 cm<sup>2</sup>.</div> <div style="border: 1px solid #ccc; padding: 2px;">Explain why this information is not reported/not relevant.</div>
Method used to determine the device area	<input checked="" type="checkbox"/> Yes <input type="checkbox"/> No	<div style="border: 1px solid #ccc; padding: 2px; margin-bottom: 2px;">The aperture area is determined by a certification laboratory.</div> <div style="border: 1px solid #ccc; padding: 2px;">Explain why this information is not reported/not relevant.</div>

#### 2. Current-voltage characterization

Current density-voltage (J-V) plots in both forward and backward direction	<input checked="" type="checkbox"/> Yes <input type="checkbox"/> No	<div style="border: 1px solid #ccc; padding: 2px; margin-bottom: 2px;">Please see the Supplementary Fig. 18 and Fig. 19.</div> <div style="border: 1px solid #ccc; padding: 2px;">Explain why this information is not reported/not relevant.</div>
Voltage scan conditions	<input checked="" type="checkbox"/> Yes <input type="checkbox"/> No	<div style="border: 1px solid #ccc; padding: 2px; margin-bottom: 2px;">The J-V curves of devices were measured both in reverse scan (2V to -0.1 V with a step of 0.013 V and a dwelling time of 10 ms at each step) and forward scan (-0.1 V to 2 V with a step of 0.013 V and a dwelling time of 10 ms at each step).</div> <div style="border: 1px solid #ccc; padding: 2px;">Explain why this information is not reported/not relevant.</div>
Test environment	<input checked="" type="checkbox"/> Yes <input type="checkbox"/> No	<div style="border: 1px solid #ccc; padding: 2px; margin-bottom: 2px;">The measurements were performed in the ambient.</div> <div style="border: 1px solid #ccc; padding: 2px;">Explain why this information is not reported/not relevant.</div>
Protocol for preconditioning of the device before its characterization	<input checked="" type="checkbox"/> Yes <input type="checkbox"/> No	<div style="border: 1px solid #ccc; padding: 2px; margin-bottom: 2px;">Please see the method part.</div> <div style="border: 1px solid #ccc; padding: 2px;">Explain why this information is not reported/not relevant.</div>
Stability of the J-V characteristic	<input checked="" type="checkbox"/> Yes <input type="checkbox"/> No	<div style="border: 1px solid #ccc; padding: 2px; margin-bottom: 2px;">Please see the manuscript Fig. 4.</div> <div style="border: 1px solid #ccc; padding: 2px;">Explain why this information is not reported/not relevant.</div>

#### 3. Hysteresis or any other unusual behaviour

Description of the unusual behaviour observed during the characterization	<input type="checkbox"/> Yes <input checked="" type="checkbox"/> No	<div style="border: 1px solid #ccc; padding: 2px; margin-bottom: 2px;">not relevant</div> <div style="border: 1px solid #ccc; padding: 2px;">Explain why this information is not reported/not relevant.</div>
Related experimental data	<input checked="" type="checkbox"/> Yes <input type="checkbox"/> No	<div style="border: 1px solid #ccc; padding: 2px; margin-bottom: 2px;">Please see the Supplementary Fig. 18 and Fig. 19.</div> <div style="border: 1px solid #ccc; padding: 2px;">Explain why this information is not reported/not relevant.</div>

#### 4. Efficiency

External quantum efficiency (EQE) or incident photons to current efficiency (IPCE)	<input checked="" type="checkbox"/> Yes <input type="checkbox"/> No	<div style="border: 1px solid #ccc; padding: 2px; margin-bottom: 2px;">The EQE spectrum was measured by a QE-R Solar Cell Spectral Response Measurement System (Enlitech).</div> <div style="border: 1px solid #ccc; padding: 2px;">Explain why this information is not reported/not relevant.</div>
A comparison between the integrated response under the standard reference spectrum and the response measure under the simulator	<input checked="" type="checkbox"/> Yes <input type="checkbox"/> No	<div style="border: 1px solid #ccc; padding: 2px; margin-bottom: 2px;">From the external quantum efficiency (EQE) spectra, the integrated JSCs are equivalent to the values acquired from the j-V curves.</div> <div style="border: 1px solid #ccc; padding: 2px;">Explain why this information is not reported/not relevant.</div>

For tandem solar cells, the bias illumination and bias voltage used for each subcell	<input checked="" type="checkbox"/> Yes <input type="checkbox"/> No	Bias illumination applied. <i>Explain why this information is not reported/not relevant.</i>
<b>5. Calibration</b>		
Light source and reference cell or sensor used for the characterization	<input checked="" type="checkbox"/> Yes <input type="checkbox"/> No	The j-V characteristics were recorded by a IV test system(ADCMT 6246) under AM1.5G dual sun intensity illumination (100 mW cm <sup>-2</sup> ) with the solar simulator (AAA Steady State Solar Simulator(SS-T155-2M). The reference cell employed was a monocrystalline silicon (mono-Si) WPVS-type device (PVM1121, NREL-certified, ISO 2098), calibrated to a short-circuit current (I <sub>sc</sub> ) of 143.95 mA under standard test conditions (STC) during the measurement session. <i>Explain why this information is not reported/not relevant.</i>
Confirmation that the reference cell was calibrated and certified	<input checked="" type="checkbox"/> Yes <input type="checkbox"/> No	The Reference cell was calibrated to a short-circuit current (I <sub>sc</sub> ) of 143.95 mA at standard test conditions (STC) during the measurement. <i>Explain why this information is not reported/not relevant.</i>
Calculation of spectral mismatch between the reference cell and the devices under test	<input checked="" type="checkbox"/> Yes <input type="checkbox"/> No	Spectral Mismatch factor was calculated and I-V correction was performed according to IEC 60891. <i>Explain why this information is not reported/not relevant.</i>
<b>6. Mask/aperture</b>		
Size of the mask/aperture used during testing	<input checked="" type="checkbox"/> Yes <input type="checkbox"/> No	The aperture area is determined by a certification laboratory. <i>Explain why this information is not reported/not relevant.</i>
Variation of the measured short-circuit current density with the mask/aperture area	<input type="checkbox"/> Yes <input checked="" type="checkbox"/> No	<i>Report the difference in the short-circuit current density values measured with the mask and aperture area.</i> <i>Explain why this information is not reported/not relevant.</i>
<b>7. Performance certification</b>		
Identity of the independent certification laboratory that confirmed the photovoltaic performance	<input checked="" type="checkbox"/> Yes <input type="checkbox"/> No	We have the certification by Shanghai Institute of Microsystem and Information Technology (SIMIT), Chinese Academy of Sciences. <i>Explain why this information is not reported/not relevant.</i>
A copy of any certificate(s)	<input checked="" type="checkbox"/> Yes <input type="checkbox"/> No	Please see the Supplementary Fig. 18 and Fig. 19. <i>Explain why this information is not reported/not relevant.</i>
<b>8. Statistics</b>		
Number of solar cells tested	<input checked="" type="checkbox"/> Yes <input type="checkbox"/> No	Please see the manuscript part. <i>Explain why this information is not reported/not relevant.</i>
Statistical analysis of the device performance	<input checked="" type="checkbox"/> Yes <input type="checkbox"/> No	Please see the manuscript part. <i>Explain why this information is not reported/not relevant.</i>
<b>9. Long-term stability analysis</b>		
Type of analysis, bias conditions and environmental conditions	<input checked="" type="checkbox"/> Yes <input type="checkbox"/> No	For maximum power point (MPP) tracking, the encapsulated devices were tested in ambient air under continuous illumination from a Xenon lamp-based solar simulator (Enli Tech, SS-F5-3A), calibrated to a light intensity of 100 mW cm <sup>-2</sup> . <i>Explain why this information is not reported/not relevant.</i>